Applied Ocean Research 76 (2018) 88–97

Contents lists available at ScienceDirect

Applied Ocean Research

journal homepage: www.elsevier.com/locate/apor

Extending DualSPHysics with a Differential Variational Inequality: modeling fluid-mechanism interaction

R.B. Canelas[a,*], M. Brito[a], O.G. Feal[b], J.M. Domínguez[b], A.J.C. Crespo[b]

[a] CERIS, Instituto Superior Técnico, ULisboa, Lisbon, Portugal
[b] EPHYSLAB, Universidade de Vigo, Ourense, Spain

ARTICLE INFO

Keywords:
SPH
DVI
Non-smooth dynamics
Multibody dynamics
Fluid–structure–structure interaction
Meshless

ABSTRACT

This work details the coupling of a Smoothed Particle Hydrodynamics (SPH) fluid solver with a general-purpose Differential Variational Inequality (DVI) based non-smooth multibody dynamics solver, allowing for efficient and accurate modeling of fluid-mechanism interactions, an ubiquitous scenario in natural and industrial settings. The SPH fluid model (DualSPHysics) can deal with flow non-linearities, free-surface and intense topological changes, while the non-smooth dynamics model (Project Chrono) deals with discontinuous frictional contacts and kinematic restrictions. An open-source integrated framework to model fluid–structure–structure coupled systems is presented by implementing Project Chrono under DualSPHysics.

The model is validated with fluid–structure–structure interaction cases. Both frictional and multi-restriction based behaviors are tested and simple convergence analysis are presented, showing that the model is capable of reproducing complex interactions. Several hypothetical cases are then presented, in order to demonstrate possible applications, showcasing a wide set of options useful for practitioners requiring the use of advanced fluid-mechanism models.

1. Introduction

Devices composed of rigid bodies interacting through frictional contacts and several nonlinear constraints are extensively used in many engineering fields, either featuring a small number of unilateral contacts or including thousands of contacts between a large number of parts. Mechanisms involving contacts and impacts between parts can be modeled in terms of multi-body systems with unilateral constraints. The simulation of rigid contacts entails the solution of non-smooth equations of motion: the dynamics are non-smooth since the non-interpenetration, collision, and adhesion constraints are discontinuous [1]. The interaction of these types of mechanisms with fluid flow is widely seen in fields such as offshore engineering, fabrication processes, coastal protection and renewable energy production.

Smoothed Particle Hydrodynamics (SPH) is becoming a mature tool regarding environmental free-surface flows. It treats unsteady and nonlinear features, extreme deformations and complex topological evolutions, such as a breaking free-surface, implicitly and with sufficient accuracy to provide meaningful solutions to engineering problems. Considerable advantages when computing interactions between objects or structures and a flow [2] are also met. High-performance computing advances have allowed the method to cover applications once reserved to specialized models, opening new possibilities in modeling even further complex phenomena. Using the same developments in computing and the introduction of accessible parallel computing solutions, very efficient solutions are found for non-smooth multi-body systems. Considering the success of SPH for fluid descriptions and non-smooth multi-body solvers for mechanical systems, attempting to couple both under a generalized framework should provide new simulation possibilities, by leveraging the strengths in both methods.

In this work the DualSPHysics code [3] is augmented with the Project Chrono library [4], developed as a general-purpose simulation framework for multi-body problems with support for very large systems. The library is implemented under the DualSPHysics code, providing an integrated interface to define and run arbitrarily defined fluid–structure–structure coupled systems. Our implementation allows for the straightforward definition of constraints such as joints (spherical, hinged and full restriction) and sliders (along an axis), combinations of these (hinged slider for example) with arbitrary degrees of freedom, i.e., such restrictions can be set between two bodies that are otherwise unrestricted. The main contribution however is the efficient treatment of such kinematic restrictions with user defined dynamic

---

[*] Corresponding author.

E-mail addresses: ricardo.canelas@tecnico.ulisboa.pt (R.B. Canelas), moises.brito@tecnico.ulisboa.pt (M. Brito), orlando@uvigo.es (O.G. Feal), jmdominguez@uvigo.es (J.M. Domínguez), alexbexe@uvigo.es (A.J.C. Crespo).

https://doi.org/10.1016/j.apor.2018.04.015
Received 21 December 2017; Received in revised form 27 March 2018; Accepted 27 April 2018

properties such as friction and restitution coefficients, restitution forces from spring and damper systems and user-imposed forces and trajectories.

The aim of this paper is to explore the DualSPHysics implementation of Project Chrono for modeling of interactions between fluid and rigid bodies systems, with arbitrary mechanical restrictions applied. The fluid implementation on DualSPHysics represents the current state-of-the-art in balancing computational efficiency and numerical accuracy, while maintaining the necessary degree of generality for users and researchers. More accurate particle approximation schemes have been introduced such as Incompressible SPH [5] and CRKSPH [6] among various others. Applicability to large and complex problems is limited however, hence they are not considered currently. The work presented is agnostic to the fluid discretization method, as well as the particulars of the fluid–solid coupling.

In Section 2 the conceptual and numerical models used for the fluid description are reviewed, mapping the equation systems underlying the DualSPHysics implementation of SPH. Section 3 introduces the concepts for the non-smooth multi-body dynamics model and the Differential Variational Inequality (DVI) equation system. Section 4 details the validation cases of the fluid-mechanism solver, using three reference experimental results. Following the validation cases, Section 5 showcases the potential of the model via a selection of cases were non-linear flows drive and interact with complex mechanisms. Conclusions are drawn in Section 6, by discussing the validation results, the usability and attractiveness of the model from a practitioner standpoint and the future developments.

2. Smooth-Particle-Hydrodynamics (SPH)

In SPH, the fluid domain is represented by a set of nodal points where physical quantities such as position, velocity, density and pressure are approximated at. These points move with the fluid in a Lagrangian manner and their properties change with time due to the interactions with neighboring nodes. The term Smoothed Particle Hydrodynamics arises from the fact that the nodes, for all intended means, carry the mass of a portion of the medium, hence being easily labeled as “particles”, and their individual angular velocity is disregarded, hence “smooth”. The method relies heavily on integral interpolant theory [7]. An approximation to discrete Lagrangian points can be made, by a proper discretisation of the continuous integral by

$$A_i \approx \sum_j A_j W(\boldsymbol{r}_{\mathrm{ij}}, h) V_j, \tag{1}$$

called the summation interpolant, extended to all particles j, $|\boldsymbol{r}_{ij}| = |\boldsymbol{r}_i - \boldsymbol{r}_j| \leq \epsilon h$, where V_j is the volume of particle j, A_i is the approximated variable at particle i and W is the weight, or kernel, function. The summation approximation implies that particle first order consistency, i.e., the ability of the kernel approximation to reproduce exactly a first order polynomial function, may not be assured, since the approximation error is inherent to the discrete form

$$\sum_j V_j W(\boldsymbol{r}_{\mathrm{ij}}, h) \approx 1 \tag{2}$$

may be large. This typically occurs near open boundaries or other discontinuities, where the kernel W does not satisfy compact support. Mitigation may be considered, as the Shepard and MLS corrections. In the work of [8] spatial gradients are computed using the gradient of the kernel function.

A Quintic [9] kernel is employed in this work:

$$W(\boldsymbol{r}_{\mathrm{ij}}, h) = \alpha_D \left(1 - \tfrac{q}{2}\right)^4 (2q + 1), \quad 0 \leq q \leq 2, \tag{3}$$

where $q = |\boldsymbol{r}_{ij}/h|$ and $\alpha_D = 21/16\pi h^3$, for a 3D case. The choice of kernel function weights on the quality of the solutions [10], with the Quintic kernel being recognized as a good choice for general free-surface problems [11].

2.1. Equations of motion in SPH

The proposed SPH formulation relies on the discretisation of the Navier–Stokes and continuity equations. Written for a variable density and neglecting the divergence of the velocity field, these are

$$\frac{d\boldsymbol{v}}{\mathrm{dt}} = -\frac{\nabla p}{\rho} + \frac{\mu}{\rho} \nabla^2 \boldsymbol{v} + \boldsymbol{g} \tag{4}$$

$$\frac{d\rho}{\mathrm{dt}} = -\rho \nabla \boldsymbol{v}, \tag{5}$$

where $\boldsymbol{v}$ is the velocity field, p is the pressure, ρ is the density and μ and g are the kinematic viscosity and body forces per unit mass, respectively. The system is written in such a way as to avoid solving a Poisson equation, using $p = f(\rho)$ [12], using a weakly compressible formulation. The continuity equation is discretised as

$$\frac{d\rho_i}{\mathrm{dt}} = \sum_j m_j (\boldsymbol{v}_i - \boldsymbol{v}_j) \cdot \nabla W(\boldsymbol{r}_{\mathrm{ij}}, h) + \Phi_i, \tag{6}$$

where m_j is the mass of particle j and Φ_i is a diffusive term [13], designed to stabilize the density field from high-frequency oscillations, written as

$$\Phi_i = 2\delta h c_0 \sum_j (\rho_j - \rho_i) \frac{\boldsymbol{r}_{\mathrm{ij}} \cdot \nabla W(\boldsymbol{r}_{\mathrm{ij}}, h)}{|r_{\mathrm{ij}}|^2} \frac{m_j}{\rho_j}, \tag{7}$$

where δ is a free parameter and c_0 is the numerical sound velocity. The discretised version of Eq. (4) [14] can be written as

$$\frac{d\boldsymbol{v}_i}{\mathrm{dt}} = -\sum_j m_j \left(\frac{p_i + p_j}{\rho_i \rho_j}\right) \nabla W(\boldsymbol{r}_{\mathrm{ij}}, h) + \boldsymbol{\Pi}_{\mathrm{ij}} + \boldsymbol{g} \tag{8}$$

The first term of the right side is a symmetrical, balanced form of the pressure term [7]. The second term represents viscous stresses, given by either an artificial viscosity formulation [7], or a laminar [15] and a sub-particle-scale (SPS) stress [16].

Following [7], the commonly used relationship estimate between pressure and density is Tait's equation

$$p_i = \frac{\rho_0 c_0^2}{\gamma} \left[\left(\frac{\rho_i}{\rho_0}\right)^{\gamma} - 1\right] \tag{9}$$

where ρ_0 is a reference density and γ = 7 for a fluid like water. According to Eq. (9), the compressibility of the fluid depends on c_0, in such a way that for a high enough sound celerity the fluid is virtually incompressible. However the value of c_0 in the model should not be the actual speed of sound, as the stability region is defined by

$$\Delta t = C \min\left[\min_i\left(\sqrt{\frac{h}{|\boldsymbol{f}_i|}}\right);\ \min_i\left(\frac{h}{c_0 + \max_j \left|\frac{\boldsymbol{v}_{\mathrm{ij}} \boldsymbol{r}_{\mathrm{ij}}}{\boldsymbol{r}_{\mathrm{ij}}^2}\right|}\right)\right], \tag{10}$$

where C is the Courant number, a constant of the order of 10^{-1} [10]. The first term results from the consideration of force magnitudes and the second is a version of the classical *CFL* condition. This expression takes into account numerical information celebrities and a restriction arising from the viscous terms [10]. If the sound celerity in the simulation is too high, it will render Δt very small and the computation more expensive. c_0 is kept to an artificial value of around 10 times the maximum flow speed, restricting the relative density fluctuations at less than 1% [7]. As a consequence, the estimated pressure field given by Eq. (9) usually shows some instabilities and may be subject to erroneous distributions. The δ-SPH diffusive terms contribute to the density field and smooth most of the high frequency oscillations.

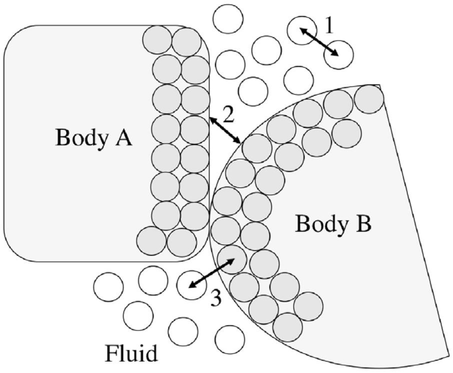

Fig. 1. Coupling scheme of a fluid and rigid body description.

2.2. Coupling rigid body dynamics and SPH

Rigid bodies are sub-sets of SPH particles whose variables are integrated in time with a different set of equations. Newton's equations for rigid body dynamics in the domain frame reference are used, and the discretization consists of summing the contributions from each SPH node, as

$$M_I \frac{d\boldsymbol{V}_I}{\mathrm{dt}} = \sum_{k\in I} m_k \frac{d\boldsymbol{v}_k}{\mathrm{dt}} \tag{11}$$

$$\boldsymbol{I}_I \frac{d\boldsymbol{\Omega}_I}{\mathrm{dt}} = \sum_{k\in I} m_k (\boldsymbol{r}_k - \boldsymbol{R}_I) \times \frac{d\boldsymbol{v}_k}{\mathrm{dt}}, \tag{12}$$

where body I possesses a mass $\boldsymbol{M_I}$, velocity $\boldsymbol{V_I}$, inertial tensor $\boldsymbol{I_I}$, angular velocity Ω_I and center of gravity $\boldsymbol{R_I}$. The vectorial quantities are computed at every time step. $m_k \frac{dv_k}{\mathrm{dt}}$ is the force by unit mass applied to particle k, belonging to body I. This force encompasses body forces (gravity) and fluid resultants. Fig. 1 details the 3 interaction types accounted for in this work.

Both interactions 1 (between fluid particles) and 3 (between fluid and boundary solid particles) are computed with Eq. (8). The model can be seen as an application of the Dynamic Boundary Conditions [17,2], where the boundary is made to additionally follow Eqs. (11) and (12). No *ad-hoc* terms are added, since all the dynamics are a result of the fundamental, particle-wise, solution of Eqs. (11) and (12). Interaction 2 is detailed in Section 3, taking place over the mesh that encompasses the boundary solid particles of each body.

The fluid–solid formulation was detailed in [2], where it was validated regarding buoyancy effects including free-surface deformation and penetration. Later works included rigid body interaction with waves and mooring lines [18] and the extensions for the Distributed Contact Discrete Element Method (DCDEM) [19] previously implemented in DualSPHysics.

3. Non-smooth multi-body dynamics model

Section 2 lays the fundamental ideas behind the modelling of the fluid phase and the modelling of otherwise unconstrained floating rigid bodies. Mechanisms to cope with interactions between rigid bodies and other constraints need to be explored. The ideas laid by [20] and later adapted by [19] represent traditional regularization strategies, which model contacts and other restrictions by means of spring-dashpot systems (DEM class methods). From a SPH implementation perspective, this approach requires small code adaptations and allows the adoption of already used integrators. The high stiffness affecting the explicit integration, however, typically imposes prohibitively small time steps to ensure stability and guarantees the need to tune parameters [21]. These issues motivate the search for methods that can deal with multiple frictional restrictions, even in cases with thousands or millions of moving bodies. To that end, much attention was drawn by time-stepping approaches that produce weak solutions of the DVI that describes the continuous time motion of rigid bodies with collision, contact, and friction, as those applied in Project Chrono. The DVI as a problem formulation was recently introduced in full generality and classified by differential index [22], though earlier numerical approaches based on DVI formulations do exist. On the following subsections, a DVI description is built by defining the notation space, writing constraints that represent physical characteristics of the system and finally writing the full equation system.

3.1. System representation

At a time t, the position of the system is described by generalized coordinates $\boldsymbol{q}(t) \in \mathbb{R}^m$ (which may include rotational coordinates that cannot be defined over a subspace homeomorphic to $\mathbb{R}^n$, for some n), and generalized velocities $\boldsymbol{v}(t) \in \mathbb{R}^m$. In classical mechanics, $\boldsymbol{v}(t)$ is continuous, and we can write $d\boldsymbol{q}/\mathrm{dt} = \boldsymbol{\Gamma}(\boldsymbol{q})\boldsymbol{v}$, where $\Gamma(\boldsymbol{q})$ is used to transform the generalized velocities into derivatives of the generalized positions. For instance, when dealing with rotations, $\Gamma(\boldsymbol{q})$ can be a linear mapping from three dimensional angular speeds into four dimensional time derivatives of unit quaternions. Four-dimensional unitary quaternions are adopted, $\boldsymbol{\eta}(t) \in S^3 \subset \mathbb{H}$, though their space is not

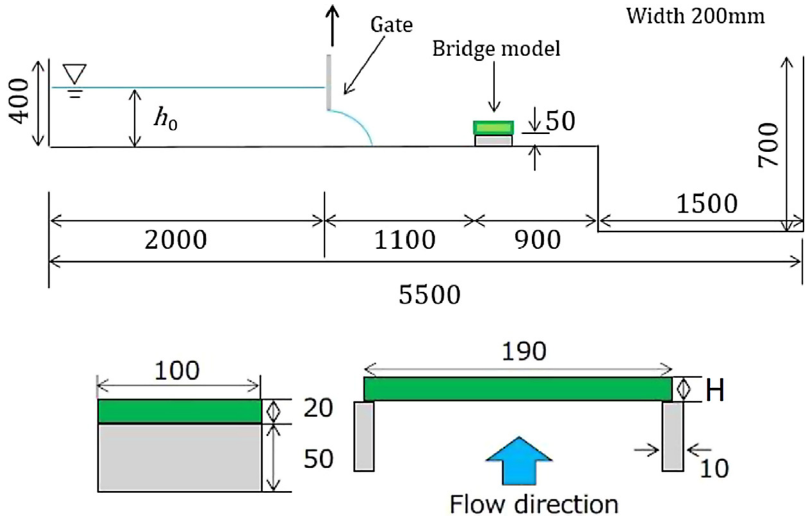

Fig. 2. Platform experimental set up scheme. Dimensions in mm [28].

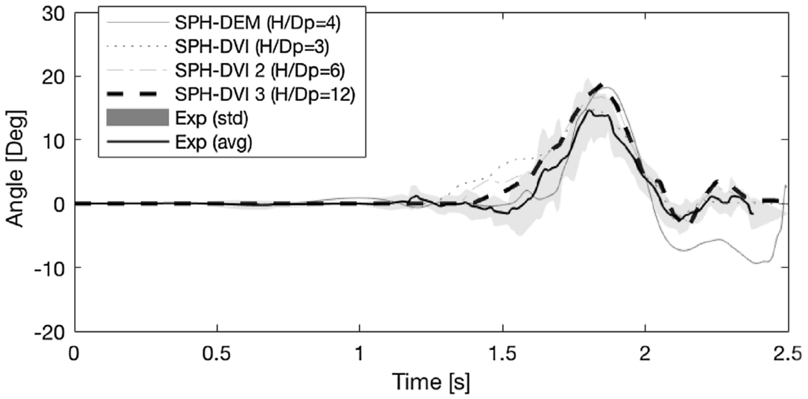

Fig. 3. Rotation angle for $h_0 = 250$ mm. Experimental (avg – average; std – standard deviation) and numerical results.

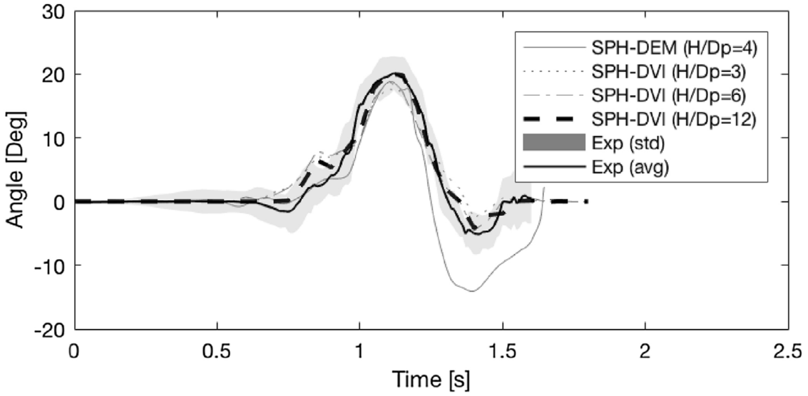

Fig. 4. Rotation angle for $h_0 = 300$ mm. Experimental (avg – average; std – standard deviation) and numerical results.

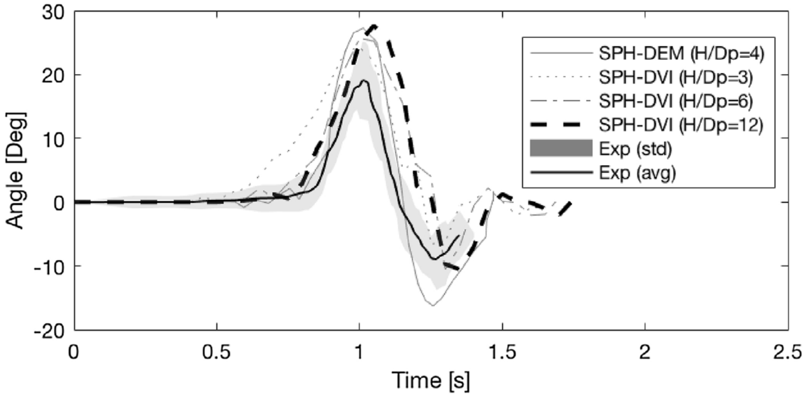

Fig. 5. Rotation angle for $h_0 = 350$ mm. Experimental (avg – average; std – standard deviation) and numerical results.

Table 1
RMSE for h_0 = [250 300 350] mm, SPH-DEM, SPH-DVI.

h_0	DEM ($H/Dp = 4$)	DVI ($H/Dp = 3$)	DVI ($H/Dp = 6$)	DVI ($H/Dp = 12$)
250 mm	1.448	1.146	0.965	0.901
300 mm	0.777	0.502	0.469	0.309
350 mm	0.941	1.188	1.276	1.355

homeomorphic to $\mathbb{R}^3$. This allows the position vector as $\boldsymbol{q} = \{\boldsymbol{x}_1^T, \boldsymbol{\eta}_1^T, \boldsymbol{x}_2^T, \boldsymbol{\eta}_2^T, \ldots\}$ and the velocity vector as $\boldsymbol{v} = \{\dot{\boldsymbol{x}}_1^T, \boldsymbol{w}_1^T, \dot{\boldsymbol{x}}_2^T, \boldsymbol{w}_2^T, \ldots\}$. Therefore a system with n bodies in three dimensions is represented by $m_p = 8n$ position and $m_s = 6n$ speed coordinates.

3.2. Non-penetration constraints

Two rigid bodies should not penetrate, and, if they are in contact, there should be friction acting at the interface. To enforce the non-penetration constraint, we assume that there exists a function $\Phi(\boldsymbol{q})$, which we call the gap function, that satisfies

$$\Phi(\boldsymbol{q}) = \begin{cases} >0 & \text{If the bodies have no intersection} \\ =0 & \text{If the bodies are in contact} \\ <0 & \text{If the bodies intersect} \end{cases} \tag{13}$$

For such a function, the non-penetration constraint becomes $\Phi(\boldsymbol{q}) \geq 0$. An example of such a mapping is the signed distance function, which is differentiable when the bodies are smooth and convex, at least up to some value of the interpenetration [23]. For most cases, even simple ones involving the relative position of two spheres, a differentiable

Table 2
Computational cost for h_0 = [250 300 350] mm, SPH-DVI.

h_0	H/Dp = 3		H/Dp = 6		H/Dp = 12	
	Million particles	Time (s)	Million particles	Time (s)	Million particles	Time (s)
250	1.88	14852	14.92	118689	105.31	787156
300	2.23	20571	17.66	159152	125.34	1423304
350	2.54	25357	20.41	204875	146.04	1580491

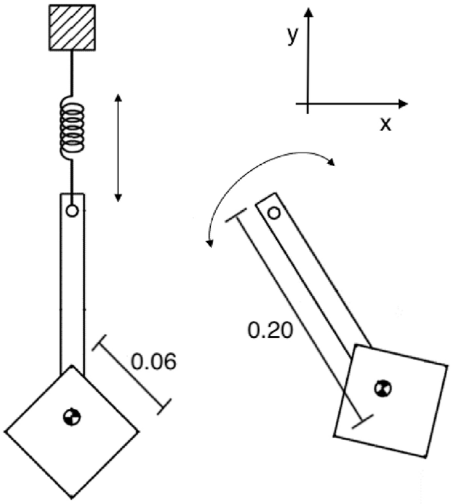

Fig. 6. Spring pendulum (left) and gravity pendulum (right). Dimensions in m.

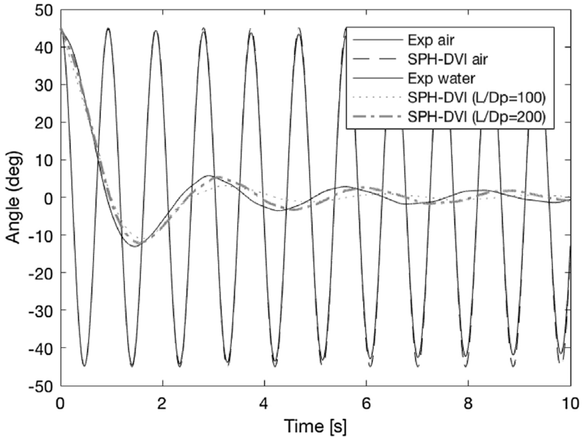

Fig. 7. Comparison between numerical and experimental [29] rotation angle of gravity pendulum in air and water.

signed distance function cannot be defined for all values of $\boldsymbol{q}$. The fact that $\Phi(\boldsymbol{q})$ can be differentially defined only in a neighborhood of the set $\Phi(\boldsymbol{q}) \geq 0$ can be accommodated at the cost of making the analysis substantially more involved [24], prompting the following assumption: any contact is described by a gap function $\Phi(\boldsymbol{q})$ that is everywhere C2.

3.3. Frictional constraints – the Coulomb friction model

The model we represent and approximate is the Coulomb friction model. If a position $\boldsymbol{q}$ is feasible and the contact is active, that is, $\Phi(\boldsymbol{q}) \geq =0$, then at the contact we have a normal force and a tangential force. Let $\boldsymbol{n}$ be the normal at the contact, pointing toward the exterior of the body, and let $\boldsymbol{t}_1$ and $\boldsymbol{t}_2$ be the tangents at the contact such that $\boldsymbol{n}$, $\boldsymbol{t}_1$ and $\boldsymbol{t}_2$ are mutually orthogonal vectors of unitary length and a function of the position $\boldsymbol{q}$. Let $\boldsymbol{v}$ to refer to velocities, and the subscripts 1 and 2 to refer to quantities related to the two linearly independent tangential directions at a given contact. The reaction force is impressed on the system by means of multipliers γ_n, γ_{v_1} and γ_{v_2}. The normal component of the force is $\boldsymbol{F}_n = \gamma_n \boldsymbol{n}$ and the tangential component of the force is $\boldsymbol{F}_t = \gamma_{v_1}\boldsymbol{t}_1 + \gamma_{v_2}\boldsymbol{t}_2$. The Coulomb model consists of the following constraints:

$$
\begin{aligned}
&\gamma_n \geq 0\\
&\Phi(\boldsymbol{q}) \geq 0\\
&\Phi(\boldsymbol{q})\gamma_n = 0\\
&\mu\gamma_n \geq \sqrt{\gamma_{v_1}^2 + \gamma_{v_2}^2}\\
&||\boldsymbol{V}_t||\left(\mu\gamma_n - \sqrt{\gamma_{v_1}^2 + \gamma_{v_2}^2}\right) = 0\\
&\langle \boldsymbol{F}_t, \boldsymbol{V}_t\rangle = -||\boldsymbol{F}_t||\ ||\boldsymbol{V}_t||
\end{aligned}
\tag{14}
$$

where $\boldsymbol{V}_t$ is the relative tangential velocity at contact. The first part of the constraint can be restated as

$$\boldsymbol{F} = \boldsymbol{F}_n + \boldsymbol{F}_t = \gamma_n \boldsymbol{n} + \gamma_{v_1}\boldsymbol{t}_1 + \gamma_{v_2}\boldsymbol{t}_2 \in \mathbb{K} \tag{15}$$

where $\mathbb{K}$ is a cone in three dimensions, whose slope is $\arctan(\mu)$. The constraint $\langle \boldsymbol{F}_t, \boldsymbol{V}_t\rangle = -||\boldsymbol{F}_t||\ ||\boldsymbol{V}_t||$ requires that the tangential force be opposite to the tangential velocity. This results in the reaction force being dissipative. In fact, an equivalent convenient way of expressing this constraint is by using the maximum dissipation principle [25]

$$(\gamma_{v_1}, \gamma_{v_2}) = \operatorname{argmin}_{\sqrt{\gamma_{v_1}^2+\gamma_{v_2}^2} \leq \mu\gamma_n} \left(\gamma_{v_1}\boldsymbol{t}_1 + \gamma_{v_2}\boldsymbol{t}_2\right)^T \boldsymbol{V}_t \tag{16}$$

These constraints are represented by mapping vectors $\boldsymbol{n}$, $\boldsymbol{t}_1$ and $\boldsymbol{t}_2$ from contact coordinates to generalized coordinates. For example, if we have a two-body system, then the generalized coordinates in the three-dimensional space are embedded in a 12-dimensional space by using the coordinates $x_1, y_1, z_1, \phi_1, \Theta_1, \zeta_1, x_2, y_2, z_2, \phi_2, \Theta_2, \zeta_2$. For a three-dimensional vector $\boldsymbol{v}$, the mapping to generalized coordinates is given by

$$\boldsymbol{v} \to \begin{pmatrix} \boldsymbol{v} \\ r_1 \times \boldsymbol{v} \\ -\boldsymbol{v} \\ -r_2 \times \boldsymbol{v} \end{pmatrix}, \tag{17}$$

where r_1 and r_2 are the relative positions of the contact point with respect to the centers of mass of the two bodies. Using this mapping, we denote the generalized vector version of $\boldsymbol{n}$, $\boldsymbol{t}_1$ and $\boldsymbol{t}_2$ by $\boldsymbol{D}_n$, $\boldsymbol{D}_1$, $\boldsymbol{D}_2$. One unfortunate side effect of generalized coordinates mapping is that, in the new coordinates, $\boldsymbol{D}_n$, $\boldsymbol{D}_1$, $\boldsymbol{D}_2$ cease to be mutually orthogonal. If u is the generalized velocity, the tangential velocity satisfies the following

$$\boldsymbol{t}_1^T \boldsymbol{V}_t = u^T \boldsymbol{D}_1, \quad \boldsymbol{t}_2^T \boldsymbol{V}_t = u^T \boldsymbol{D}_2 \tag{18}$$

In generalized coordinates, the Coulomb model can now be written as

$$
\begin{aligned}
&F_n = \gamma_n \boldsymbol{D}_n\\
&F_t = \gamma_{v_1}\boldsymbol{D}_1 + \gamma_{v_2}\boldsymbol{D}_2\\
&\gamma_n \geq 0, \quad \Phi(\boldsymbol{q}) \geq 0, \quad \Phi(\boldsymbol{q})\gamma_n = 0\\
&\mu\gamma_n \geq \sqrt{\gamma_{v_1}^2 + \gamma_{v_2}^2}\\
&(\gamma_{v_1}, \gamma_{v_2}) = \operatorname{argmin}_{\sqrt{\gamma_{v_1}^2+\gamma_{v_2}^2} \leq \mu\gamma_n} (\gamma_{v_1}\boldsymbol{D}_1 + \gamma_{v_2}\boldsymbol{D}_2)^T u
\end{aligned}
\tag{19}
$$

3.4. Complete non-smooth multi-body dynamics model

The other dynamical data needed for the model are the mass matrix $\boldsymbol{M}(\boldsymbol{q})$ and the external force $\boldsymbol{f}_e(t, \boldsymbol{q}, \boldsymbol{v})$. The mass matrix $\boldsymbol{M}(\boldsymbol{q}) \in \mathbb{R}^{m\times m}$ is positive definite and constant. Assuming now that we have p potential contact constraints, which are enforced by the nonpenetration constraints $\Phi^i(\boldsymbol{q}) \geq 0$, $i = 1, 2, .. ., p$. The superscript i denotes the data associated to the potential contact i. The continuous model is the following differential variational inequality [26]

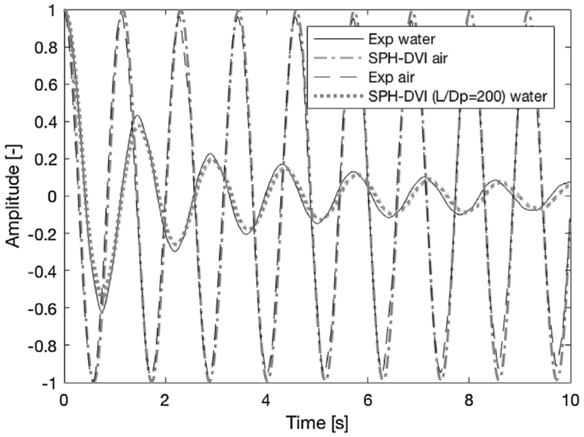

Fig. 8. Comparison between numerical and experimental [29] motion amplitude of a spring pendulum in air and water.

$$
\begin{aligned}
&\frac{d\boldsymbol{q}}{\mathrm{dt}} = \boldsymbol{\Gamma}(\boldsymbol{q})\boldsymbol{v}\\
&\boldsymbol{M}\frac{d\boldsymbol{v}}{\mathrm{dt}} = \sum_{i=1}^{p}(\gamma_n^i\boldsymbol{D}_n^i + \gamma_{v_1}^i\boldsymbol{D}_1^i + \gamma_{v_2}^i\boldsymbol{D}_2^i) + \boldsymbol{f_e}(t, \boldsymbol{q}, \boldsymbol{v})\\
&\gamma_n^i \geq 0 \quad \perp\Phi^i(\boldsymbol{q}) \geq 0, \quad i = 1, 2, \ldots, p\\
&(\gamma_{v_1}^i, \gamma_{v_2}^i) = \operatorname{argmin}_{\sqrt{\gamma_{v_1}^{i\ 2} + \gamma_{v_2}^{i\ 2}} \leq \mu^i\gamma_n^i}(\gamma_{v_1}^i\boldsymbol{D}_1^i + \gamma_{v_2}^i\boldsymbol{D}_2^i)^T u,\\
&i = 1, 2, \ldots, p
\end{aligned}
\tag{20}
$$

System (20) must be discretized for use in our numerical model. Casting the system in Cone Complementary Problem (CCP) form and solving it with a fixed point iterative method allows for the expected performance levels, while taking advantage of the DVI capabilities in describing generalized restrictions. The full discretization can be seen in Project Chrono's reference papers, [27,4].

4. Validation cases

4.1. Platform wash-out by dam break

A simply supported platform is exposed to a dam break flow, leading to the collapse and partial transport of the structure by the flow. [28] presented experimental data for such a scenario and compared it with an SPH-DEM coupled model.

The case consists of three different initial water depths: $h_0 = \{250, 300, 350\}$ mm. The simply supported platform has a density of $\rho = 1.161\ \mathrm{kg/m^3}$ and is made of PLA plastic, with a restitution coefficient $e = 0.8$ and friction coefficient to the supports $\mu = 0.05$. Fig. 2 details the set-up.

The SPH-DVI simulations were conducted on the same domain, at the same scale. Resolution ranged as $H/Dp = \{3, 6, 12\}$, where H is the height to the platform (20 mm). Artificial viscosity [7] with $\alpha = 0.01$ was used and the δ-SPH parameter was set to $\delta = 0.1$. Figs. 3–5 show the rotation angle of the supported block on the axis normal to the flow direction, compared to the experimental and the SPH-DEM solutions from [28], taken with $H/Dp = 4$, where Dp is the initial particle spacing.

The frictional nature of the support problem is well reproduced by the exact Coulomb model of Eq. (19), as well as the subsequent motion of the platform. The times for movement initiation are consistent, as are the angle inversion times. Minor differences are noted for increased resolution, indicating that solid–fluid coupling is robust, as well as a proper decoupling of the solid–solid problem from the fluid–solid model, resolution wise. Regarding the comparison with the DEM results, Table 1 shows the root mean square error (RMSE) for the three cases and the four solutions.

Overall the error is comparable for similar resolutions and decreases with increased resolution, sub-linearly. Besides the greater accuracy, the DVI model has two more advantages: (I) it effectively decouples the solid–solid interaction from the fluid resolution, arguably the most expensive part of the solution and (II) it has a much larger stability region than explicit DEM models, allowing for larger time-steps.

The computational time is relative to the available machine, in this case an Nvidia P100 GPU card was used along an Intel Xeon E5, allowing for large number of particles to be stored. Table 2 shows the computational time and particle numbers for the presented case.

The computational time is the same for a case with no DVI model enabled, i.e., the cost of the DVI solution is negligible.

4.2. Pendulums in viscous fluids

A set of pendulum experiments were recovered from [29] in order to characterize of the SPH-DVI solutions regarding fluid-mechanism interactions, i.e. structures with relative internal restrictions. The tests consist of optically tracking a submerged PVC cube with a protruding rod. The cube side is $L = 0.06$ m and the rod extends 0.20 m from the cube center, with a 23.5×2 mm cross section, resulting in a total system mass of 0.29 kg.

The system can be set-up with either a hinge (gravity pendulum) or a spring (spring pendulum) at the top of the rod as shown in Fig. 6, producing rotational (around the xy axis) and translational motion (along the y axis), respectively, once the mechanism is excited.

The simulations were carried with a 1:1 scale, using $\delta = 0.1$ for the δ-SPH model and $\nu = 10^{-6}$ for the viscosity employed in the

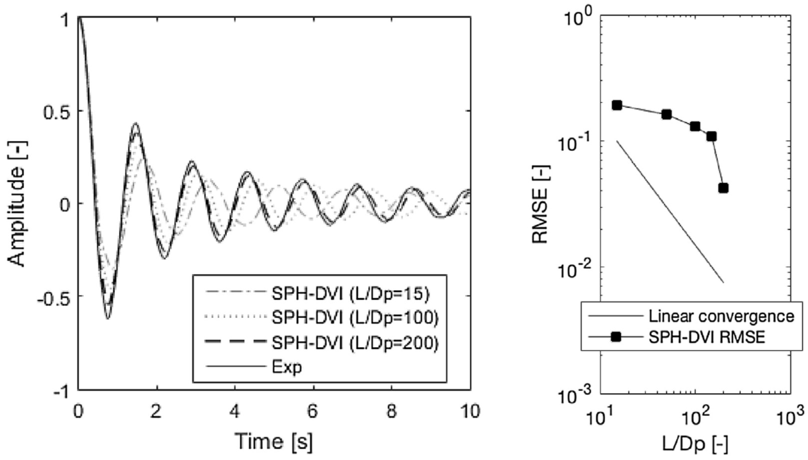

Fig. 9. Left – Comparison between numerical and experimental [29] motion amplitude of a spring pendulum in water. Right – Convergence analysis for Dp = [15, 50, 100, 150, 200].

Table 3

Computational cost for H/Dp = [15 100 200].

H/Dp	Million particles	Time (s)
15	0.05	212
100	15.63	59684
200	125.48	478972

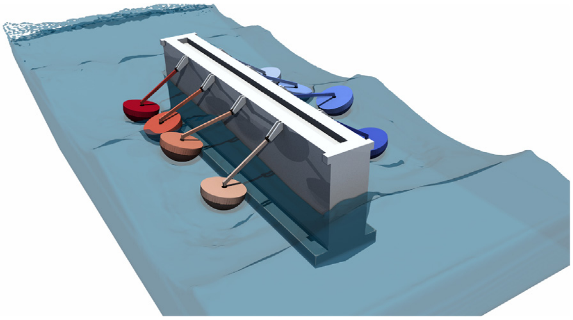

Fig. 10. WaveStar DualSPHysics simulation.

Laminar + SPS model. The air phase is not modeled by the SPH + DVI approach. Fig. 7 shows the angular rotation of the gravity pendulum in air and water.

The gravity pendulum presents a 1.073 Hz natural frequency in air, with a 1.73×10^{-3} damping ratio. The effectiveness of the DVI approach is demonstrated by exactly reproducing frequency. The amplitude shows a deviation from the experimental results: the motion damping introduced by air resistance and friction at the hinge is not characterized by [29] and hence not modeled. The DVI solution presents a negligible damping ratio ($\sim 10^{-6}$), possibly due to machine precision. The introduction of fluid promotes a higher energy dissipation, resulting in a lower natural frequency and increased damping ratios. The SPH-DVI solution is shown to converge to the experimental solution, with approximately 7% error in amplitude and 6% error in frequency for a resolution of L/Dp = 200.

The spring pendulum uses a spring with a stiffness of 8.72 N/m, resulting in a 0.874 Hz frequency, with a 0.681×10^{-3} damping ratio in air. Fig. 8 compares the normalized experimental and SPH-DVI results.

The solution for the air case is again accurate in both amplitude and frequency, apart from the damping. Results for the submerged case show good agreement for the most resolved case, with L/Dp = 200. Fig. 9 details the effects of varying resolution and shows a convergence analysis.

Approximately linear convergence is expected by the SPH method [30]. The convergence analysis in Fig. 9 shows, for a limited resolution bandwidth, two regions with sublinear and superlinear convergence rates. Given the characteristics of the problem, this is to be expected: major flow structures such as eddies largely contribute to systems response. These may be under-resolved for resolutions much lower than their spatial scale, and the case under scrutiny presents a given significant eddy size, relatable to the local Reynold number. Above a given cut off resolution, these now resolved structures greatly contribute for the convergence of the results. The dissipative nature of the SPH

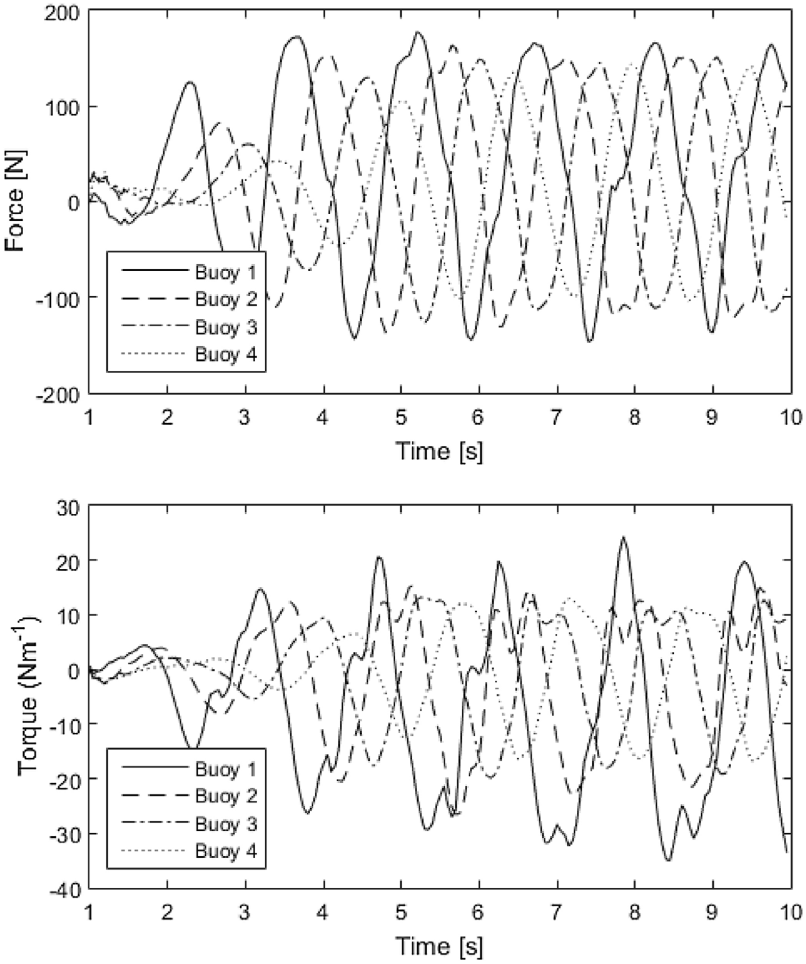

Fig. 11. WaveStar buoy vertical force and torque response with no PTO.

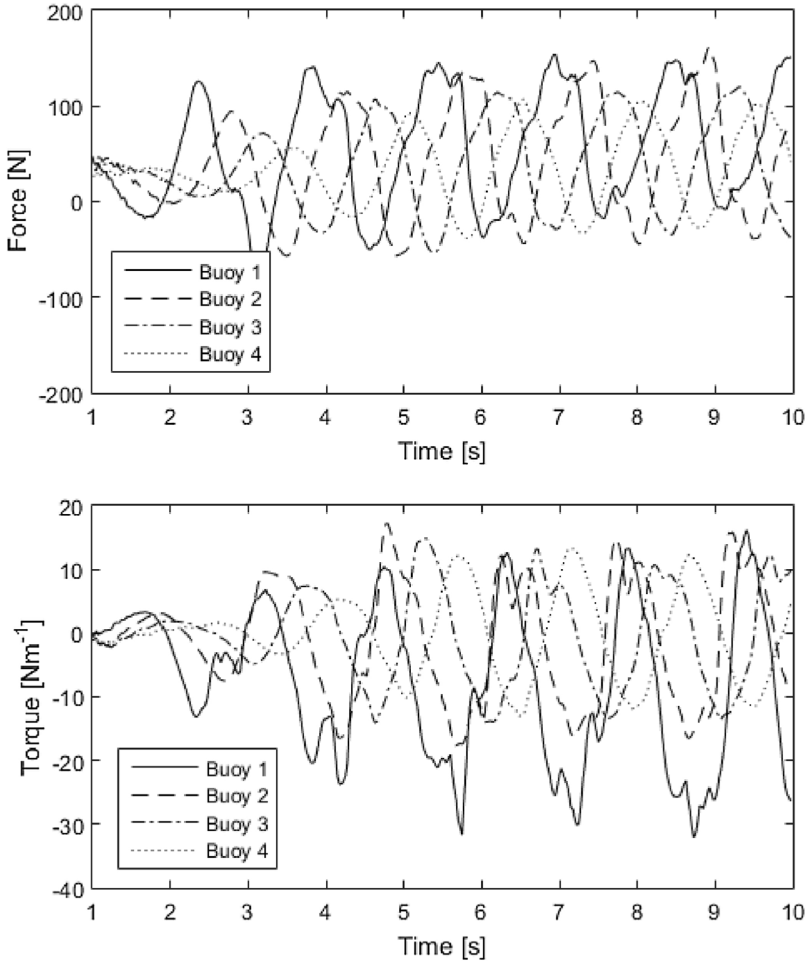

Fig. 12. WaveStar buoy force and torque response with PTO.

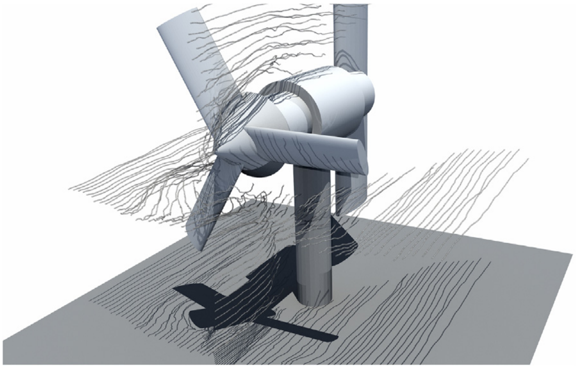

Fig. 13. Passive tidal turbine in DualSPHysics.

method [7] implies that high resolution is necessary to fully recover the correct damping ratios, with multi-resolution schemes [31] being important to offset the computational cost for larger applications. Table 3 details the said cost, for the described reference machine.

5. Demonstration cases

In order to demonstrate the versatility of the DualSPHysics implementation of Project Chrono, three demonstration cases are presented. These explore different types of restrictions (spherical, hinged) and varied conditions, with relative and absolute restrictions.

5.1. WaveStar

The WaveStar machine (wavestarenergy.com) was idealized as a wave energy converter (WEC) consisting of a row of half-submerged buoys, as shown in Fig. 10.

The oscillatory motion of the buoys as a wave passes is harnessed for energy production with a power take-off system (PTO) that uses the rotation speed of the arm connected to the buoy. A fundamental design concern with this type of machine is the efficiency loss due to shadow effects on the series of buoys. Under normal operating conditions a trivial linear analysis model can be used to recover the machine response, but non-linear models or experimental set-ups are required to analyze extreme conditions. DualSPHysics can now fully describe the system and perform the integrated multiphysics computations.

A regular wave-maker was initialized, generating 2nd order waves of the same amplitude as the height of the buoys ($H = 0.45\,\mathrm{m}$) and a frequency of 0.65 Hz, resulting in a wavelength of $\approx 4\,\mathrm{m}$. For a non-damped mechanism, i.e., with a disengaged PTO, the force and torque responses on the buoys are represented in Fig. 11.

The first buoy is clearly more excited, with the expected influence of the shadow being apparent in the signal from the following buoys. A PTO can be added by incorporating a non-linear spring that resists the rotation of the arm, at the connection to the main body. Forces and torques for such a case are represented in Fig. 12, corresponding to a spring with stiffness $k = 2500\,\mathrm{Nm}^{-1}$, damping coefficient $\nu = 500\,\mathrm{Nsm}^{-1}$ and non-linear stiffness exponent $p = 1.25$.

Comparing both quantities for both cases, the amplitudes in the damped case are smaller, as expected, with the signals presenting more

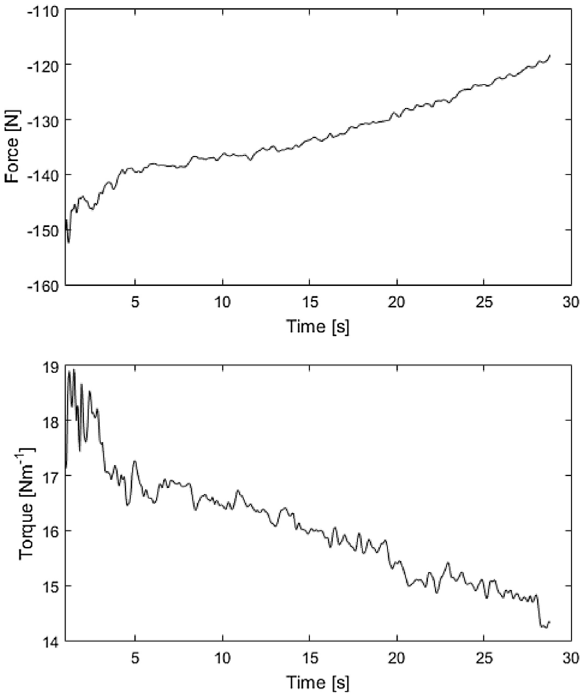

Fig. 14. Passive tidal turbine in DualSPHysics. Reaction force and torque at the pillar joint with non-uniform tide.

variability and apparent shadow effects being more pronounced. The 10 s simulations were carried out in under 155 min, with a resolution of approximately 20 particles per buoy diameter.

5.2. Tidal turbine

Tidal turbines are typically designed as bottom attached machines that take advantage of tidal currents to activate a PTO. Dynamics are typically very slow, and the direction of the turbine is decided by an active controller, designed to optimize energy production. In the following simulations a fully passive design is presented, no control over the turbine orientation is exerted, instead using a large hydrodynamic foil to align the turbine with the flow. A snapshot of the solution can be seen in Fig. 13.

The central pillar allows for the body of the turbine to rotate on the vertical axis, while the propeller is allowed to rotate along the axis of the body, with both joints fully undamped. The foil is visible at the end of the turbine body. The scenario consists of a zero to approximately one tenth body length per second average fluid velocity, along a 30 s interval, recreating a sudden tidal surge. The horizontal reaction force and torque on the pillar joint are shown in Fig. 14.

Both force and torque show the expected decrease as the propeller begins to rotate and disturb the developing flow, decreasing the drag forces. The design of the foil can be optimized under varied performance objectives and flow conditions with simple geometric changes, with computational times of approximately 130 min for a resolution of 12 particles for the pillar diameter.

5.3. Ragdoll

Considering the amount of interlocking joints, self-collision possibilities and overall geometry, the human articulations are a challenging mechanical system to reproduce, let alone in the context of a fully coupled fluid–solid solver. Fig. 15 shows the set-up of a dam-break on an irregular geometry were a fully jointed dummy ragdoll was placed. The shoulders, hips and neck are represented by spherical restrictions, while elbows and knees are hinged rotations. No explicit limits were placed on the extent of the relative rotations, a possibility with the current implementation. The model is fully self-colliding, using the full description of the DVI approach described in Eq. (20).

The case was run on a Nvidia GTX Titan Black, counted 4.4 million particles and the 10 s simulation took 41 h to run, due to the high resolution. A case without the ragdoll took 37 h, and the added cost is related to the collision detection.

6. Conclusions

A multi-physics augmented version of DualSPHysics was presented, by implementing part of Project Chrono's library, namely, the DVI solver. This allows for general fluid and mechanism descriptions to be coupled, presenting simulation and analysis possibilities previously unattainable, unless custom implementations were developed. The validation tests show that the model reproduces both frictional and

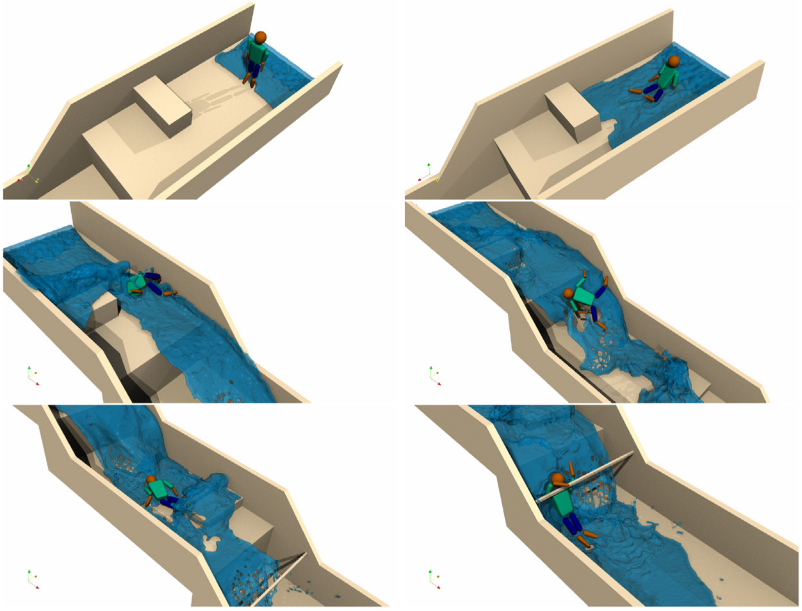

Fig. 15. Sequential instants of a Ragdoll simulation in DualSPHysics. t = 1, 2, 5, 6.5, 7.5 and 9 s.

mechanical constraints, appearing to converge at the rate of the employed SPH method. Further work on resolution refinement for the fluid discretization should provide the quality of the higher resolution configurations with a fraction of the computational cost.

The application cases were designed to showcase the potential of the model pertaining to scenarios were a fully coupled, non-linear model is fundamental to correctly reproduce the system. Use of the new model is trivial, since the preprocessing pipeline for DualSPHysics is employed. Due to the efficiency of the DVI formulation, impact on the computational time is residual, allowing for large and complex systems to be modeled with ease. These cases represent real applications were GPU accelerated SPH can have great impact on optimization and design guidelines for relevant industries. Further work will see the increase in available joint topologies, as well as the inclusion of structural analysis by employing Project Chrono's FEM solver, as well as explore adaptive resolution schemes [31] and particle shifting algorithms [5] to increase the solution accuracy while decreasing computational cost.

Acknowledgements

This work was partially supported by the EU and Portuguese Foundation for Science (FCT), in the frame of the collaborative international consortium STEEPSTREAMS financed under the ERA-NET Cofund WaterWorks2014 Call, project WaterJPI/0006/2014. This ERA-NET is an integral part of the 2015 Joint Activities developed by the Water Challenges for a Changing World Joint Programme Initiative (Water JPI). Partial support was also given by Xunta de Galicia under project ED431C 2017/64 Programa de Consolidación e Estructuración de Unidades de Investigación Competitivas (Grupos de Referencia Competitiva) co-funded by European Regional Development Fund (FEDER) and the Ministry of Economy and Competitiveness of the Government of Spain under project WELCOME ENE2016-75074-C2-1-R.

References

[1] A.A. Shabana, Dynamics of Multibody Systems, Cambridge University Press, 2005, http://dx.doi.org/10.1017/cbo9780511610523.

[2] R. Canelas, J. Domínguez, A. Crespo, M. Gómez-Gesteira, R. Ferreira, A smooth particle hydrodynamics discretization for the modelling of free surface flows and rigid body dynamics, Int. J. Numer. Methods Fluids 78 (2015) 581–593.

[3] A. Crespo, J. Domínguez, B. Rogers, M. Gómez-Gesteira, S. Longshaw, R. Canelas, R. Vacondio, A. Barreiro, O. García-Feal, Dualsphysics: open-source parallel CFD solver on smoothed particle hydrodynamics (SPH), Comput. Phys. Commun. 187 (2015) 204–216.

[4] A. Tasora, M. Anitescu, A matrix-free cone complementarity approach for solving large-scale, Nonsmooth Rigid Body Dyn. 200 (5) (2011) 439–453.

[5] S. Lind, R. Xu, P. Stansby, B. Rogers, Incompressible smoothed particle hydrodynamics for free-surface flows: a generalised diffusion-based algorithm for stability and validations for impulsive flows and propagating waves, J. Comput. Phys. 231 (4) (2012) 1499–1523. Available: http://www.sciencedirect.com/science/article/pii/S0021999111006279.

[6] N. Frontiere, C.D. Raskin, J.M. Owen, CRKSPH – a conservative reproducing kernel smoothed particle hydrodynamics scheme, J. Comput. Phys. 332 (2017) 160–209.

[7] J. Monaghan, Smoothed particle hydrodynamics, Rep. Prog. Phys. 68 (8) (2005) 1703. Available: http://stacks.iop.org/0034-4885/68/i = 8/a = R01.

[8] A. Colagrossi, M. Landrini, Numerical simulation of interfacial flows by smoothed particle hydrodynamics, J. Comput. Phys. 191 (2003) 448–475.

[9] H. Wendland, Piecewise polynomial, positive definite and compactly supported radial functions of minimal degree, Adv. Comput. Math. 4 (1) (1995) 389–396, http://dx.doi.org/10.1007/BF02123482.

[10] M. Gómez-Gesteira, B. Rogers, A.R. Dalrymple, A. Crespo, State-of-the-art of classical SPH for free-surface flows, J. Hydraul. Res. 48 (2010) 6–27, http://dx.doi.org/10.1080/00221686.2010.9641242.

[11] F. Macia, A. Colagrossi, M. Antuono, A. Souto-Iglesias, Benefits of using a Wendland kernel for free-surface flows, 6th ERCOFTAC SPHERIC Workshop on SPH Applications, Hamburg University of Technology, 2011, pp. 30–37.

[12] E. Lee, D. Violeau, R. Issa, S. Ploix, Application of weakly compressible and truly incompressible SPH to 3D water collapse in waterworks, J. Hydraul. Res. 48 (2010).

[13] D. Molteni, A. Colagrossi, A simple procedure to improve the pressure evaluation in hydrodynamic context using the SPH, Comput. Phys. Commun. 180 (2009) 861–872.

[14] R. Dalrymple, B. Rogers, Numerical modeling of water waves with the SPH method, Coast. Eng. 53 (2–3) (2006) 141–147. Available: http://www.sciencedirect.com/science/article/pii/S0378383905001304.

[15] J.P. Morris, P.J. Fox, Y. Zhu, Modeling low Reynolds number incompressible flows using SPH, J. Comput. Phys. 136 (1) (1997) 214–226. Available: http://www.sciencedirect.com/science/article/pii/S0021999197957764.

[16] H. Gotoh, T. Shibahara, T. Sakai, Sub-particle-scale turbulence model for the MPS method – Lagrangian flow model for hydraulic engineering, Adv. Methods Comput. Fluid Dyn. 9–4 (2001) 339–347.

[17] A.J.C. Crespo, M. Gomez-Gesteira, R.A. Dalrymple, Boundary conditions generated by dynamic particles in SPH methods, Comput. Mater. Contin. 5 (3) (2007) 173–184.

[18] A. Barreiro, A. Crespo, J. Dominguez, O. Garcia-Feal, I. Zabala, M. Gomez-Gesteira, Quasi-static mooring solver implemented in SPH, J. Ocean Eng. Mar. Energy 2 (3) (2016) 381–396.

[19] R. Canelas, A. Crespo, J. Domínguez, R. Ferreira, M. Gómez-Gesteira, SPH-DCDEM model for arbitrary geometries in free surface solid–fluid flows, Comput. Phys. Commun. 202 (2016) 131–140.

[20] A.V. Potapov, M.L. Hunt, C.S. Campbell, Liquid-solid flows using smoothed particle hydrodynamics and the discrete element method, Powder Technol. 116 (2–3) (2001) 204–213. Available: http://www.sciencedirect.com/science/article/pii/S0032591000003958.

[21] H. Kruggel-Emden, E. Simsek, S. Rickelt, S. Wirtz, V. Scherer, Review and extension of normal force models for the discrete element method, Powder Technol. 171 (3) (2007) 157–173. Available: http://www.sciencedirect.com/science/article/pii/S0032591006004360.

[22] J.-S. Pang, D.E. Stewart, Differential variational inequalities, Math. Program. 113 (2) (2008) 345–424, http://dx.doi.org/10.1007/s10107-006-0052-x.

[23] M. Anitescu, F.A. Potra, Formulating dynamic multi-rigid-body contact problems with friction as solvable linear complementarity problems, Nonlinear Dyn. 14 (3) (1997) 231–247.

[24] M. Anitescu, G.D. Hart, A constraint-stabilized time-stepping approach for rigid multibody dynamics with joints, contact and friction, Int. J. Numer. Methods Eng. 60 (14) (2004) 2335–2371.

[25] D.E. Stewart, Rigid-body dynamics with friction and impact, SIAM Rev. 42 (1) (2000) 3–39.

[26] J.-S. Pang, D.E. Stewart, Differential variational inequalities, Math. Program. 113 (2) (2008) 345–424.

[27] M. Anitescu, A. Tasora, An iterative approach for cone complementarity problems for nonsmooth dynamics, Comput. Optim. Appl. 47 (2) (2010) 207–235.

[28] B. Chandra, M. Asai, Verification and validation of the fluid-rigid body interaction simulation by the smoothed particle hydrodynamics method, Proceedings of Computational Engineering Conference JSCES 21 (2016).

[29] M. Arnold, M. Kretschmer, J. Koch, P.W. Cheng, F. Biskup, et al., A validation method for fluid–structure-interaction simulations based on submerged free decay experiments, The Twenty-Fifth International Ocean and Polar Engineering Conference, International Society of Offshore and Polar Engineers, 2015.

[30] Q. Zhu, L. Hernquist, Y. Li, Numerical convergence in smoothed particle hydrodynamics, Astrophys. J. 800 (1) (2015) 6.

[31] R. Vacondio, B. Rogers, P. Stansby, P. Mignosa, J. Feldman, Variable resolution for SPH: a dynamic particle coalescing and splitting scheme, Comput. Methods Appl. Mech. Eng. 256 (2013) 132–148.